frontiers in Materials

ORIGINAL RESEARCH
published: 14 February 2022
doi: 10.3389/fmats.2022.823192

Probing the Damage Recovery Mechanism in Irradiated Stainless Steels Using *In-Situ* Microcantilever Bending Test

*Keyou S. Mao[1], Hao Wang[2], Haozheng J. Qu[3], Kayla H. Yano[4], Philip D. Edmondson[1], Cheng Sun[5] and Janelle P. Wharry[3]**

[1]Materials Science and Technology Division, Oak Ridge National Laboratory, Oak Ridge, TN, United States, [2]Western Digital Corporation, San Jose, CA, United States, [3]School of Materials Engineering, Purdue University, West Lafayette, IN, United States, [4]Energy and Environment Directorate, Pacific Northwest National Laboratory, Richland, WA, United States, [5]Advanced Characterization and PIE, Idaho National Laboratory, Idaho Falls, ID, United States

Single crystalline microcantilevers are fabricated from the base metal and heat-affected zone (HAZ) of a laser welded, neutron irradiated austenitic stainless steel, for scanning electron microscope (SEM) *in-situ* bending. In the HAZ, cantilevers exhibit higher yield point and lower crack tip blunting displacement than in the base metal and unirradiated archive specimen. These results suggest that radiation-induced defects harden the base metal, whereas the HAZ exhibits annealing of defects leading to mechanical softening. Dislocation nucleation ahead of the crack tip is responsible for ductile blunting behavior and provides a pathway to mitigating helium-induced cracking during weld repairs of irradiated materials.

Keywords: irradiation, helium, laser weld, microcantilever, crack

OPEN ACCESS

Edited by:
Konstantina Mergia, National Centre of Scientific Research Demokritos, Greece

Reviewed by:
Ning Guo, Southwest University, China
Pavlo Maruschak, Ternopil Ivan Pului National Technical University, Ukraine

****Correspondence:***
Janelle P. Wharry
jwharry@purdue.edu

Specialty section:
This article was submitted to Mechanics of Materials, a section of the journal Frontiers in Materials

Received: *26 November 2021*
Accepted: *11 January 2022*
Published: *14 February 2022*

Citation:
Mao KS, Wang H, Qu HJ, Yano KH, Edmondson PD, Sun C and Wharry JP (2022) Probing the Damage Recovery Mechanism in Irradiated Stainless Steels Using In-Situ *Microcantilever Bending Test. Front. Mater. 9:823192. doi: 10.3389/fmats.2022.823192*

INTRODUCTION

Life extensions of commercial light water nuclear reactors (LWRs) require damage-free crack repairs in both in-core and near-core structural components. These weld repairs face challenges from the high helium (He) content, which can cause bubbles and cracks in structural materials following intense neutron irradiation (Morishima et al., 2004; Yamada et al., 2006). If conventional welding methods are used, the high temperature in the welding pool and the tensile stress developed upon cooling facilitate He bubble growth and exacerbates the intergranular He-induced cracking (HeIC) at the weld pool boundaries in the heat affected zone (HAZ) (Nishimura et al., 1998; Asano et al., 1999; Kanne et al., 1999). Low heat input welding technologies such as laser welding have been proposed to limit HeIC in previously irradiated materials, but the crack growth and arrest mechanisms are not well understood, especially given that the irradiated materials exhibit highly localized deformation. Previous studies have shown the effects of hydrogenation on fracture toughness and damage mechanisms in reactor steels, where microplastic deformation initiates the brittle failure dependent on the hydrogen, temperature and stress conditions (Yasniy et al., 2011; Yasniy et al., 2013).

Additionally, probing the interface between the base metal and weld HAZ can be difficult with traditional mechanical testing methods. Recent advancements in micromechanical testing enable *in-situ* observation of real-time mechanical response to environmental stimuli (Ding et al., 2014; Gong et al., 2015; Ast et al., 2017; Hosemann, 2018; Barnoush et al., 2019; Mao et al., 2020a). Specifically, microcantilever bending has been used to determine hydrogen embrittlement with respect to hydrogen-induced cracking (Deng et al., 2017; Deng and Barnoush, 2018); quantify the fracture toughness and dislocation structures of brittle materials through site-specific investigation

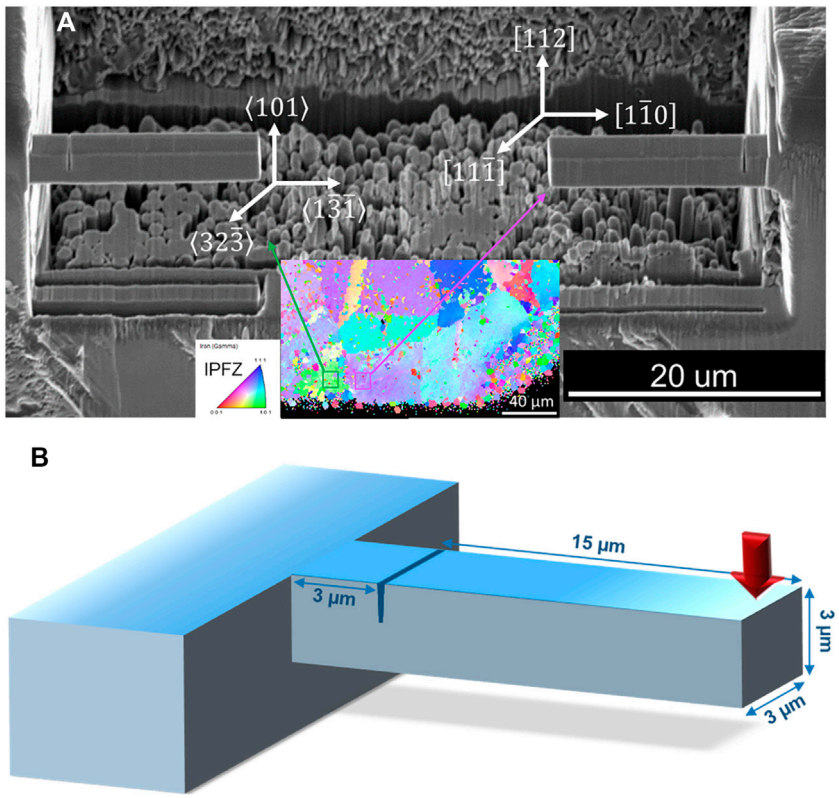

FIGURE 1 | (A) Fabricated microcantilevers in the archive material. The left cantilever is single crystalline with respect to bending direction <101> and the right cantilever is oriented towards <112> (IPFZ). **(B)** Schematic diagram of the dimensions of each microcantilever.

in thin films, single crystals, and grain boundaries (Iqbal et al., 2012; Zou et al., 2017; Alfreider et al., 2018; Ast et al., 2018; Ast et al., 2019); and probe the mechanical impact on ion-irradiated damage layers (Armstrong et al., 2015; Leide et al., 2020; Yano et al., 2020). HeIC initiation and propagation can also be investigated using site-specific micromechanical tests, where small-scale heterogeneity of structures and properties are prevalent, analogous to the irradiated materials (Diaz De La Rubla et al., 2000; Byun et al., 2006; Cui et al., 2018a), representing a manifestation of the localized mechanical degradation with an underlying irradiation-induced microstructure that is present at even finer scale such as clusters and channels (Patra and McDowell, 2013; Cui et al., 2018b; Cui et al., 2018c; Wharry et al., 2019).

In this study, we use a state-of-the-art scanning electron microscope (SEM) *in-situ* testing of microcantilevers fabricated from the base metal and HAZ in laser welds of irradiated 304L austenitic stainless steel. The cantilever bending experiments aim to probe the crack growth and propagation behavior of the base metal compared to the HAZ. Accompanying finite element analysis (FEA) models plastic strain near the crack tip during bending. Together, the microcantilevers coupled with FEA models enable precise determination of deformation mechanisms as a function of plastic strain and grain orientation. The initial microstructure without deformation is also characterized to provide insights on the structure-property relationships, which can guide improvements to the integrity and quality of laser welding technologies to extend the life of LWRs.

MATERIALS AND METHODS

The materials used for this work were AISI 304L SS with ~5–10% cold work. Samples were neutron irradiated in Experimental Breeder Reactor II at ~415°C to a total dose level of ~1 displacement per atom (dpa), and He concentration of 0.2 atomic parts per million (appm), representing 0.2% swelling. The history of these specimens can be found in previous studies (Wiezorek et al., 2014; Huang et al., 2015; Freyer et al., 2019). Irradiated samples were polished to metallographic standards inside the Westinghouse Materials Centers of Excellence hot cells. Then, single-pass pulsed laser welds were made along the length of the surfaces of the specimens. The Trumpf BEO D70 laser welding head was equipped with a TruPulse 556 pulsed Nd:YAG laser and an Alabama laser wire feeder with 6.35 mm diameter ER308L SS weld filler material. The laser welding parameters were consistent with those reported in previous studies (Mao et al., 2020b; Mao et al., 2020c; Mao et al., 2021), where the laser power was 1.4 kW, travel speed was 64 mm/min, wire feed speed was 432 mm/min, and lens-to-work distance was 200 mm. Laser welding was performed on the irradiated specimens to alter the irradiated microstructure in the HAZ, including the

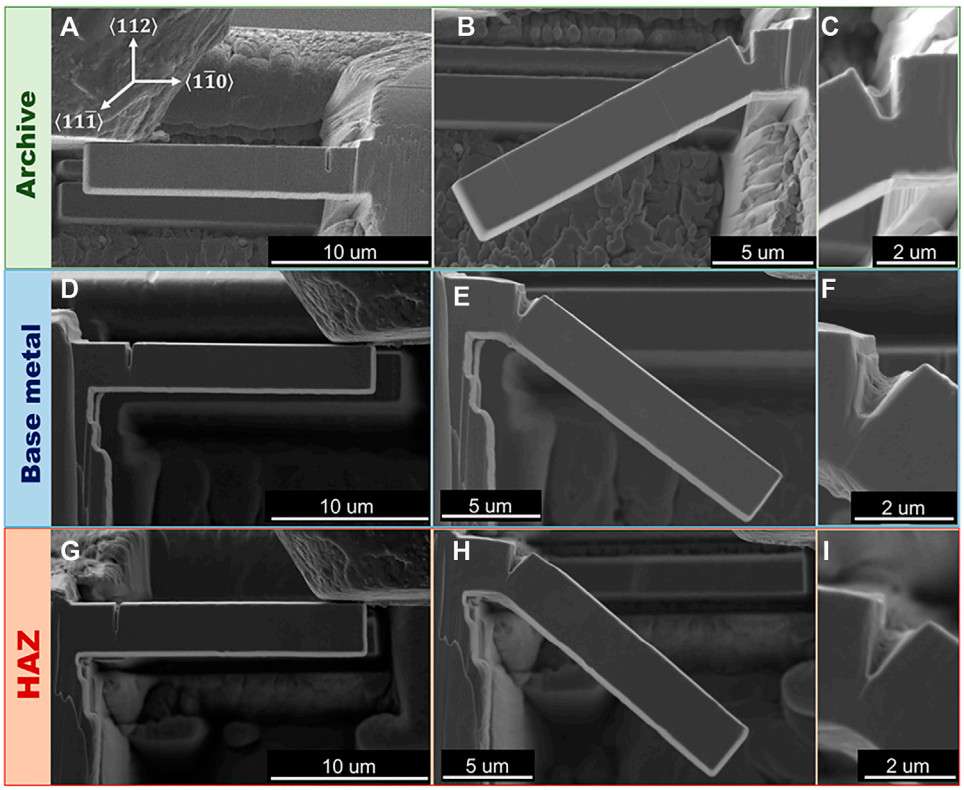

FIGURE 2 | Detailed images captured on the notch evolution before **(A,D,G)** and after **(B,C,E,F,H,I)** bending tests in the archive material (a–c), irradiated base metal **(D–F)**, and irradiated HAZ **(G–I)**.

cavities, dislocations, and precipitates. The as-welded samples were cross-sectioned, then polished using standard metallographic methods to minimize surface effects prior to microcantilever testing and microscopy characterization. The unirradiated archive material was used as a reference control.

A FEI (now Thermo Fisher Scientific) Quanta 3D FEG dual-beam SEM/focused ion beam (FIB) was used for fabricating microcantilevers and subsequently preparing FIB lift-outs for transmission electron microscopy (TEM) and scanning TEM (STEM) characterization. This FIB microscope was also equipped with an electron backscatter diffraction (EBSD) detector to collect orientation imaging microscopy (OIM) maps of grains to select single-crystal locations for microcantilever manufacturing. The OIM map in **Figure 1** and **Supplementary Figure S1** shows two examples of selecting grains oriented parallel to the microcantilever bending direction with respect to the inverse pole figure in Z (IPFZ corresponds to the upward arrow). The average grain size

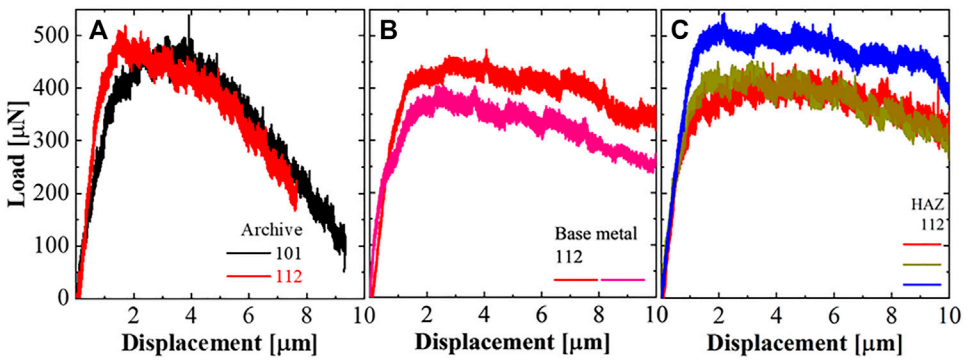

FIGURE 3 | Load versus displacement curves for the microcantilevers in the **(A)** archive specimen, and **(B)** base metal and **(C)** HAZ region of the irradiated specimen. The legend indicates the bending direction of each cantilever.

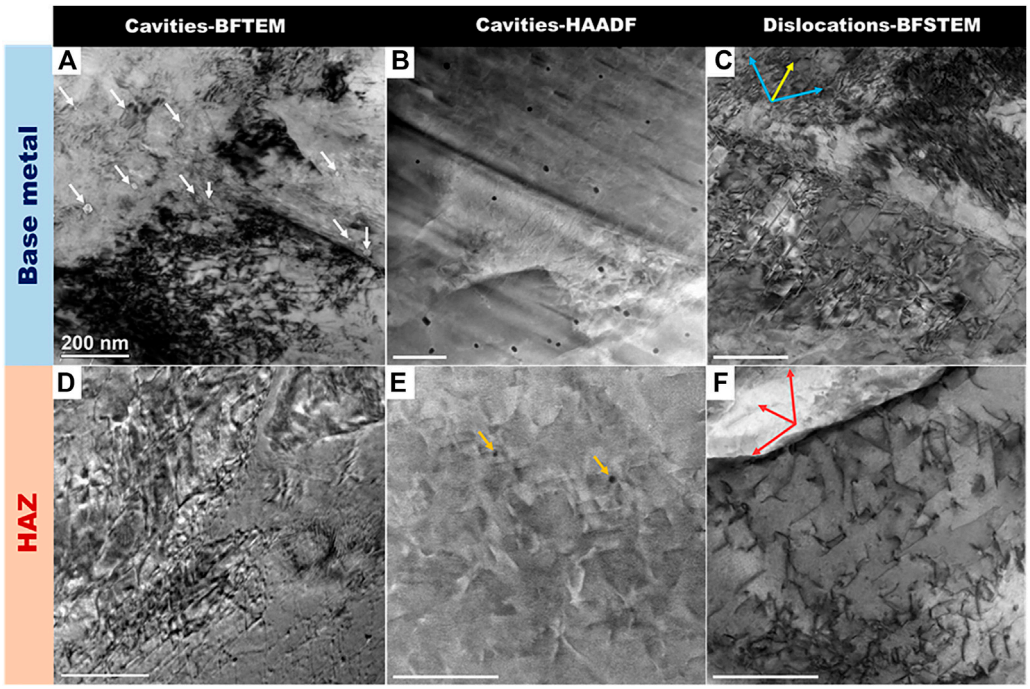

FIGURE 4 | Microstructure of the irradiated base metal **(A–C)** and HAZ **(D–F)**. **(A,D)** BFTEM of cavities in the under-focused condition; **(B,E)** HAADF of cavities, showing HAZ has fewer cavities than the base metal; **(C,F)** dislocation structure using on-zone BFSTEM imaging technique. Blue arrows represent <111> directions, yellow arrows represent <002> directions and red arrows represent <101> directions. All scale bars represent 200 nm in length.

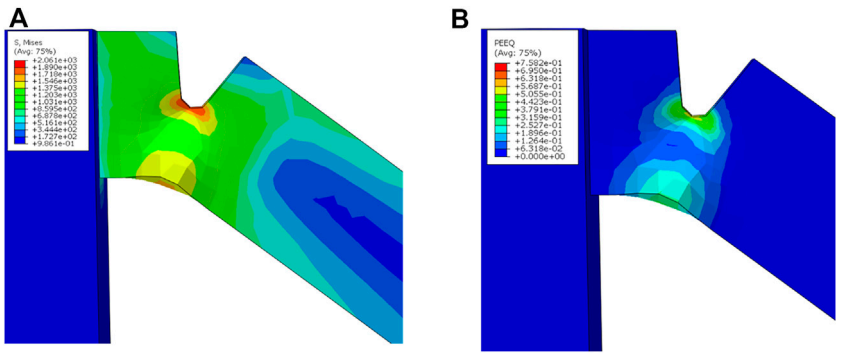

FIGURE 5 | FEA simulation on the microcantilever bending, showing **(A)** von Mises stress map and **(B)** equivalent plastic strain maps near the notch tip.

of the archive materials is 52 ± 17.7 μm. After laser welding, the welded zone has an average grain size of 27.5 ± 11.7 μm, while the average grain size of the base metal and HAZ is 47.6 ± 2.5 and 49.1 ± 4.2 μm (**Supplementary Figure S1**). Single grains were selected for SEM *in-situ* microcantilever bending tests in both the base metal and HAZ. Because the specimen is a dissimilar weld, we only focus on the HAZ and base, where the base metal is selected as far as possible away from the HAZ (see the supplementary materials for more details). Microcantilever bending experiments were conducted on the base metal, HAZ, and archive specimen with the notch oriented along the <112> direction; an archive specimen with notch oriented along <101> was also tested. **Figure 1A** illustrates the microcantilever configuration using the archive specimen as an example. The cantilever on the left-hand side of the image is made from a single crystal with respect to the bending direction <101> and the cantilever on the right-hand side of the image is oriented towards <112>. Standard FIBing process was employed to mill two to four microcantilevers of dimensions ~3 × 3 × 15 μm (length is the measured distance to the notch) per grain orientation. The notch depth ranged between 1 and 2 μm (see **Figure 1B**). The final cleaning step applied a 0.1 nA beam at 30 kV to minimize surface ion damage. Each cantilever was bent using a flat punch in the Bruker Hysitron PI-88 depth-sensing *in-*

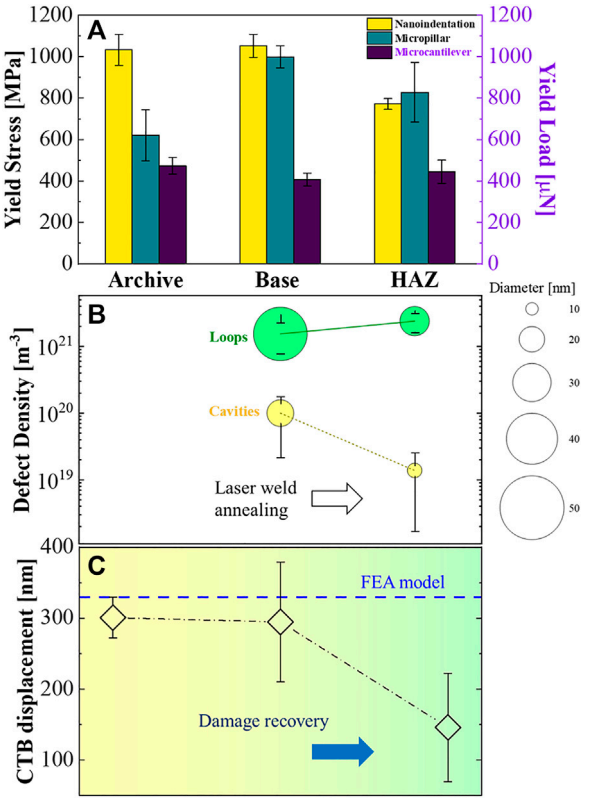

FIGURE 6 | Microstructure-mechanical property relationships across the irradiated base metal and HAZ with respect to the archive control specimen (Mao, 2019; Mao et al., 2019; Mao et al., 2020b). **(A)** Yield stress measured by nanoindentation and micropillar compression experiments. **(B)** Comparison of size and number density of dislocation loops and cavities in the base metal and HAZ. **(C)** Comparison of experimentally measured and FEA predicted crack tip blunting displacement.

situ SEM mechanical testing holder, operating at ambient temperature. The compression was carried out in displacement-controlled mode with a speed of 100 nm/s. The maximum displacement was ~10 μm. Load-displacement curves were recorded by the PI-88 with real-time video during each bending test.

A Tecnai TF30-FEG STWIN S/TEM was used to characterize the pre-deformation microstructures. TEM lamellae were prepared by FIB milling to dimensions of approximately 10 μm × 10 μm × 100 nm. A final 5 kV cleaning step was conducted to remove the residual FIB damage. Irradiation-induced cavities were imaged using both the bright-field TEM (BFTEM) and STEM modes with a high-angle annular dark-field (HAADF) detector. Dislocation structure was captured by a bright-field STEM (BFSTEM) method with small collection and convergence angles (Parish et al., 2015). The irradiation-induced precipitates were not distinguished from the loops in both the base metal and HAZ, and their number density is low enough to be excluded. The thickness of the TEM specimens was measured by electron energy loss spectroscopy (EELS). The calculated EELS mean-free-path was 90 nm. The average number densities of cavities and dislocation loops were calculated by counting the area density of the defects in each micrograph (~7–10 images include a total of ~900–1,500 features), and then divided by the measured thickness of the specimen.

The microcantilever bending test was also modeled using 3-D finite element mesh built in ABAQUS/CAE 6.14–2 (**Supplementary Figure S2**). The dimensions of the simulated microcantilever were identical to those created experimentally and described in **Figure 1B**. The indenter was modeled as a 3-D analytical rigid object with the cone angle $\theta = 60^{\circ}$. The contact between the indenter and the microcantilever is modeled as hard contact without penetration and friction, with a contact length of 3 μm as measured from **Figure 1**. Hexahedron elements (C3D8) were used for the microcantilever with a size of 0.5 μm. Wedge elements (C3D6) with a size of 0.05 μm were used around the notch tip. The elastoplastic material properties of AISI 304L SS from literature (Mao et al., 2020c; Kweon et al., 2021) were used in the model. Displacement controlled loading was applied on the simulated indenter equivalent to that used in the experiment (~10 μm).

RESULTS AND DISCUSSION

Representative images of the notch evolution captured during the bending tests are given in **Figures 2A–I** for the archive, base metal, and HAZ specimens, respectively. The highest magnification images of the post-bend tested notch (**Figures 2C,F,I**) indicate no crack tip growth or extension in either the archive, base metal, or HAZ specimens, respectively. The *in-situ* microcantilever bending videos further verify that no crack tip propagation or opening has occurred during the bending tests, which is consistent with the *post-mortem* images of the crack tip.

The representative load versus displacement curves for the microcantilevers is presented in **Figure 3**. No statistically significant variation in yield point is observed across all specimens, with average yield points being highest in the archive specimen at 473 ± 40 (**Figure 3A**), lowest in the irradiated base metal at 407 ± 31 (**Figure 3B**), and 445 ± 56 for the irradiated HAZ (**Figure 3C**). The displacement at yield is also consistent across all specimens. Finally, there do not appear to be significant differences in yield point between the <101> and <112> directions of the archive specimen.

The differences in the yield load across all three regions indicate the initial (pre-deformation) microstructure plays a role in affecting the mechanical response, especially in the irradiated specimen. **Figure 4** shows the microstructure of the base metal (**Figures 4A–C**) and HAZ (**Figures 4D–F**). BFTEM images are taken on cavities in under-focused conditions (**Figures 4A,D** and **Supplementary Figure S3**). HAADF-STEM images were also given as a complementary approach to capture the irradiation-induced cavities (**Figures 4B,E**). Dislocation structure using on-zone BFSTEM imaging technique is shown in **Figures 4C,F**. Blue arrows represent <111> directions, yellow arrows represent <002> directions and red arrows represent <101> directions. In general, the HAZ has a lower density of cavities

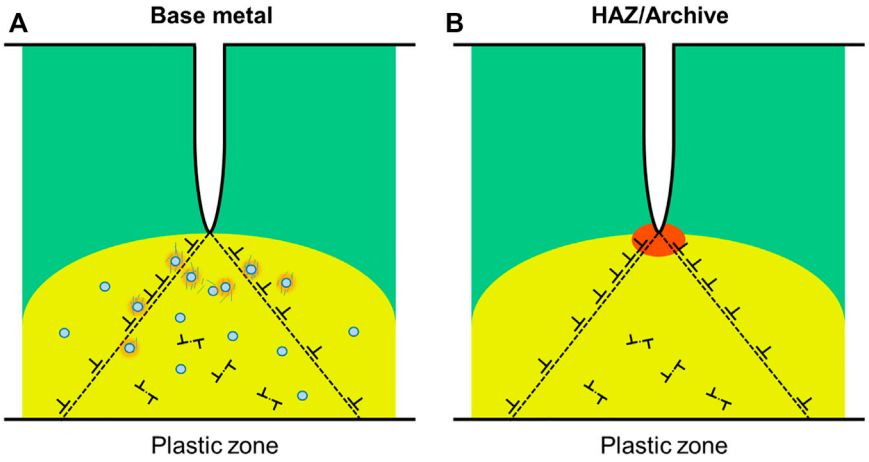

FIGURE 7 | Schematic representation of the crack tip blunting mechanisms plastic zone ahead of the crack tip. **(A)** Base metal has a higher density of cavities which could activate martensitic transformation. **(B)** Since only crack blunting occurs during bending, the plastic zone under the crack tip is represented by the yellow region as ductile behavior with an orange-highlighted stress concentration area immediately ahead of the crack and dislocations nucleates from the crack tip as well as active sources.

and similar density of dislocation loops compared to the base metal, which is consistent to our previous studies (Mao et al., 2020b; Mao et al., 2021).

FEA simulated von Mises stress and equivalent plastic strain maps are shown in **Figures 5A,B**. During loading, high tensile stress is induced around the notch tip, leading to a large plastic deformation zone. At the same time, the bottom surface of the microcantilever deforms under compressive stress. The maximum von Mises stress appears in front of the notch tip, which also shows the highest stress triaxiality. Due to the high ductility of the material, instead of forming and propagating cracks, the notch tip opens and blunts.

Figure 6 compares the microstructure-mechanical property relationships of the base metal, HAZ, and archive control specimen, across multiple micromechanical testing configurations presented herein and from previous studies (Mao, 2019; Mao et al., 2019; Mao et al., 2020b). **Figure 6A** shows that the yield stress measured by both nanoindentation (yellow) and micropillar compression (dark green) experiments are reversely correlated to the yield load measured by microcantilevers (purple). As is shown in **Figure 3**, the base metal has the highest yield stress, whereas the HAZ has the lowest yield load. This could be explained by the localized structure in the HAZ induced by laser welding, consistent with the reported post-irradiation annealing on irradiation-induced cavities in other metal and alloy systems (Byun et al., 2014; Gao et al., 2018; Mao et al., 2020c). **Figure 6B** provides evidence on the damage recovery using a bubble plot (legend shows the average diameter of the dislocation loop/cavity) on the defect density of dislocation loops and cavities in the base metal and HAZ. It is evident that the HAZ has a lower number density of cavities than the base metal. Moreover, laser-weld induced finer microstructure such as stacking faults (**Supplementary Figure S4**) could also contribute to the yield point increase in the HAZ, analogous to the enhanced mechanical strength and fracture toughness associated with thermally annealed nanotwins (Qin et al., 2009; Xiong et al., 2016; Xiong et al., 2018) (note that the blue curve from the HAZ in **Figure 3C** has the highest yield point among all the cantilever bending tests). Crack tip blunting (CTB) displacement is determined from the *in-situ* microcantilever bending tests by measuring the difference between the pre- and post-bending notch tip (**Figure 6C**). The notch tip opening width is 330 nm in the FEA simulation, which is close to experimental observations (Archive: 301 ± 29 nm, Base metal: 295 ± 84 nm, HAZ: 146 ± 76 nm). Despite the differences of the CTB between the base metal and HAZ, the ductile facture mode during the plastic deformation along with no microcracks in the HAZ (Mao et al., 2021) suggests the factual brittle transition temperature (DBTT) of the weldment is less than the maximum allowable component-specific DBTT (Katona, 2013).

The crack blunting behavior is illustrated schematically in **Figure 7**, which shows ductile behavior in the plastic zone under the crack tip with a localized region of stress concentration immediately ahead of the crack. Dislocations likely nucleate or glide towards the crack tip-cross-slip driven or dislocation multiplication mechanism (Bitzek and Gumbsch, 2013; Daly et al., 2017; Ast et al., 2019) as well as active sources such as heterogeneities generated by extreme conditions (Lucas, 1993; Sun et al., 2021). In the base metal (**Figure 7A**), the existence of radiation-induced cavities could activate the martensitic transformation near cavities through shear deformation (Yang et al., 2022). However, in the HAZ or the archive materials (**Figure 7B**), dislocations are active sources for slip and work hardening. This difference in the fracture toughness through martensitic transformation has both been demonstrated by atomistic simulation (Grujicic et al., 1997) and ASTM standard tests (Haghgouyan et al., 2019), where the phase transformation could decrease the fracture toughness. Even though no fracture toughness could be directly measured in our microcantilever bending experiments, the presence of martensite near cavities in the base metal could facilitate the crack blunting, leading to a higher displacement of CTB shown in

Figure 6C. Moreover, the post-mortem fractograms in **Figure 2** indicate the beginning of the quasistatic separation at the crack tip notch, which has been observed in electrolytic hydrogen-treated steels in WWER-440 reactor as "ductile separation mechanism" (dimple-shaped surface) (Yasniy et al., 2013). In summary, the microstructure-property relationship suggests that HeIC can be alleviated through the laser welding process, which creates an annealed HAZ microstructure that behaves in a more ductile manner than the irradiated base metal.

CONCLUSION

In this work, we present the crack tip blunting behavior of notched microcantilevers fabricated from the base metal versus HAZ in a laser welded, neutron irradiated 304 austenitic stainless steel. Both experimental and simulation results indicate that the thermal annealing induced by laser welding limits crack tip extension at low He concentrations, which mitigates HeIC. The reduction of the CTB of the HAZ compared to the base metal by ~50% suggests a ductile plastic deformation with a damage recovery mechanism. This study highlights the unique role of micromechanical experiments for more accurate prediction of the properties and damage mechanisms of nuclear structural materials under extreme irradiation and weld conditions.

DATA AVAILABILITY STATEMENT

The datasets presented in this study can be found in online repositories. The names of the repository/repositories and accession number(s) can be found in the article/ **Supplementary Material**. Additional data supporting the conclusion of this can be found in the GitHub repository https://github.com/keyoumao/Microcantilever

AUTHOR CONTRIBUTIONS

KM: Writing-original and draft, experimentation, data curation, analysis and modeling. HW: FEA modeling, data validation, manuscript revision. HQ: FEA and data curation and validation. KY: FEA modeling. PE: Supervision and manuscript revision. CS: Funding acquisition, supervision. JW: Project administration, conceptualization, funding acquisition, supervision.

FUNDING

This work was supported by the Idaho National Laboratory Directed Research and Development (LDRD) Program under U.S. Department of Energy (DOE) Idaho Operations Office Contract DE-AC07-051D14517. This work was also supported by U.S. Department of Energy, Light-Water Reactor Sustainability Program of the Office of Nuclear Energy, under contract number DE-AC-05-00OR22725. Specimens were generated through support from the U.S. DOE Office of Nuclear Energy contract DE-NE0008525 with complementary Nuclear Science User Facilities (NSUF) access. This manuscript has been authored by UT-Battelle, LLC, under contract DE-AC05-00OR22725 with the US Department of Energy (DOE).

ACKNOWLEDGMENTS

We would like to thank Fei Teng, David Frazer, Jatu Burns, Bryan Forsman and James Madden at Idaho National Laboratory (INL) for their assistance with microscopy and sample preparation. We also would like to thank Lin Shao and Frank Garner at Texas A&M University for specimen shipment and handling. The publisher acknowledges the US government license to provide public access under the DOE Public Access Plan (http://energy.gov/downloads/doe-public-access-plan)

SUPPLEMENTARY MATERIAL

The Supplementary Material for this article can be found online at: https://www.frontiersin.org/articles/10.3389/fmats.2022.823192/full#supplementary-material

REFERENCES

Alfreider, M., Kozic, D., Kolednik, O., and Kiener, D. (2018). *In-situ* Elastic-Plastic Fracture Mechanics on the Microscale by Means of Continuous Dynamical Testing. *Mater. Des.* 148, 177–187. doi:10.1016/j.matdes.2018.03.051

Armstrong, D. E. J., Hardie, C. D., Gibson, J. S. K. L., Bushby, A. J., Edmondson, P. D., and Roberts, S. G. (2015). Small-scale Characterisation of Irradiated Nuclear Materials: Part II Nanoindentation and Micro-cantilever Testing of Ion Irradiated Nuclear Materials. *J. Nucl. Mater.* 462, 374–381. doi:10.1016/j.jnucmat.2015.01.053

Asano, K., Nishimura, S., Saito, Y., Sakamoto, H., Yamada, Y., Kato, T., et al. (1999). Weldability of Neutron Irradiated Austenitic Stainless Steels. *J. Nucl. Mater.* 264, 1–9. doi:10.1016/s0022-3115(98)00491-7

Ast, J., Mohanty, G., Guo, Y., Michler, J., and Maeder, X. (2017). *In Situ* micromechanical Testing of Tungsten Micro-cantilevers Using HR-EBSD for the Assessment of Deformation Evolution. *Mater. Des.* 117, 265–266. doi:10.1016/j.matdes.2016.12.052

Ast, J., Polyakov, M. N., Michler, J., Maeder, X., and Maeder, X. (2018). Interplay of Stresses, Plasticity at Crack Tips and Small Sample Dimensions Revealed by *In-Situ* Microcantilever Tests in Tungsten. *Mater. Sci. Eng. A* 710, 400–412. doi:10.1016/j.msea.2017.10.096

Ast, J., Ghidelli, M., Durst, K., Göken, M., Sebastiani, M., and Korsunsky, A. M. (2019). A Review of Experimental Approaches to Fracture Toughness Evaluation at the Micro-scale. *Mater. Des.* 173, 107762. doi:10.1016/J.MATDES.2019.107762

Barnoush, A., Hosemann, P., Molina-Aldareguia, J., and Wheeler, J. M. (2019). *In Situ* small-scale Mechanical Testing under Extreme Environments. *MRS Bull.* 44, 471–477. doi:10.1557/MRS.2019.126

Bitzek, E., and Gumbsch, P. (2013). Mechanisms of Dislocation Multiplication at Crack Tips. *Acta Materialia* 61, 1394–1403. doi:10.1016/J.ACTAMAT.2012.11.016

Byun, T. S., Hashimoto, N., Farrell, K., and Lee, E. H. (2006). Characteristics of Microscopic Strain Localization in Irradiated 316 Stainless Steels and Pure Vanadium. *J. Nucl. Mater.* 349, 251–264. doi:10.1016/J.JNUCMAT.2005.10.011

Byun, T. S., Baek, J.-H., Anderoglu, O., Maloy, S. A., and Toloczko, M. B. (2014). Thermal Annealing Recovery of Fracture Toughness in HT9 Steel after Irradiation to High Doses. *J. Nucl. Mater.* 449, 263–272. doi:10.1016/J.JNUCMAT.2013.07.064

Cui, Y., Po, G., and Ghoniem, N. (2018a). Size-Tuned Plastic Flow Localization in Irradiated Materials at the Submicron Scale. *Phys. Rev. Lett.* 120, 215501. doi:10.1103/PHYSREVLETT.120.215501/FIGURES/4/MEDIUM

Cui, Y., Po, G., and Ghoniem, N. (2018b). Suppression of Localized Plastic Flow in Irradiated Materials. *Scripta Materialia* 154, 34–39. doi:10.1016/J.SCRIPTAMAT.2018.04.046

Cui, Y., Po, G., and Ghoniem, N. M. (2018c). A Coupled Dislocation Dynamics-Continuum Barrier Field Model with Application to Irradiated Materials. *Int. J. Plasticity* 104, 54–67. doi:10.1016/J.IJPLAS.2018.01.015

Daly, M., Burnett, T. L., Pickering, E. J., Tuck, O. C. G., Léonard, F., Kelley, R., et al. (2017). A Multi-Scale Correlative Investigation of Ductile Fracture. *Acta Materialia* 130, 56–68. doi:10.1016/j.actamat.2017.03.028

Deng, Y., and Barnoush, A. (2018). Hydrogen Embrittlement Revealed via Novel *In Situ* Fracture Experiments Using Notched Micro-cantilever Specimens. *Acta Materialia* 142, 236–247. doi:10.1016/J.ACTAMAT.2017.09.057

Deng, Y., Hajilou, T., Wan, D., Kheradmand, N., and Barnoush, A. (2017). *In-situ* Micro-cantilever Bending Test in Environmental Scanning Electron Microscope: Real Time Observation of Hydrogen Enhanced Cracking. *Scripta Materialia* 127, 19–23. doi:10.1016/J.SCRIPTAMAT.2016.08.026

Diaz de la Rubia, T., Zbib, H. M., Khraishi, T. A., Wirth, B. D., Victoria, M., and Caturla, M. J. (2000). Multiscale Modelling of Plastic Flow Localization in Irradiated Materials. *Nature* 406, 871–874. doi:10.1038/35022544

Ding, R., Gong, J., Wilkinson, A. J., and Jones, I. P. (2014). ⟨c+a⟩ Dislocations in Deformed Ti-6Al-4V Micro-cantilevers. *Acta Materialia* 76, 127–134. doi:10.1016/J.ACTAMAT.2014.05.010

Freyer, P. D., Tatman, J. K., Garner, F. A., Frederick, G. J., and Sutton, B. J. (2019). "Hot Cell Pulsed Laser Welding of Neutron Irradiated Type 304 Stainless Steel with a Maximum Damage Dose of 28 DPA,". *Codes and Standards* (San Antonio, Texas, USA: American Society of Mechanical Engineers), Vol. 1, 1–13. doi:10.1115/PVP2019-93316

Gao, J., Huang, H., Liu, X., Wang, C., Stubbins, J. F., and Li, Y. (2018). A Special Coarsening Mechanism for Intergranular Helium Bubbles upon Heating: A Combined Experimental and Numerical Study. *Scripta Materialia* 147, 93–97. doi:10.1016/J.SCRIPTAMAT.2018.01.006

Gong, J., Benjamin Britton, T., Cuddihy, M. A., Dunne, F. P. E., and Wilkinson, A. J. (2015). ⟨a⟩ Prismatic, ⟨a⟩ Basal, and ⟨c+a⟩ Slip Strengths of Commercially Pure Zr by Micro-cantilever Tests. *Acta Materialia* 96, 249–257. doi:10.1016/J.ACTAMAT.2015.06.020

Grujicic, M., Lai, S. G., and Gumbsch, P. (1997). Atomistic Simulation Study of the Effect of Martensitic Transformation Volume Change on Crack-Tip Material Evolution and Fracture Toughness. *Mater. Sci. Eng. A* 231, 151–162. doi:10.1016/S0921-5093(97)00068-3

Haghgouyan, B., Hayrettin, C., Baxevanis, T., Karaman, I., and Lagoudas, D. C. (2019). Fracture Toughness of NiTi-Towards Establishing Standard Test Methods for Phase Transforming Materials. *Acta Materialia* 162, 226–238. doi:10.1016/J.ACTAMAT.2018.09.048

Hosemann, P. (2018). Small-scale Mechanical Testing on Nuclear Materials: Bridging the Experimental Length-Scale gap. *Scripta Materialia* 143, 161–168. doi:10.1016/j.scriptamat.2017.04.026

Huang, Y., Wiezorek, J. M. K., Garner, F. A., Freyer, P. D., Okita, T., Sagisaka, M., et al. (2015). Microstructural Characterization and Density Change of 304 Stainless Steel Reflector Blocks after Long-Term Irradiation in EBR-II. *J. Nucl. Mater.* 465, 516–530. doi:10.1016/j.jnucmat.2015.06.031

Iqbal, F., Ast, J., Göken, M., and Durst, K. (2012). *In Situ* micro-cantilever Tests to Study Fracture Properties of NiAl Single Crystals. *Acta Materialia* 60, 1193–1200. doi:10.1016/j.actamat.2011.10.060

Kanne, W. R., Louthan, M. R., Rankin, D. T., and Tosten, M. H. (1999). Weld Repair of Irradiated Materials. *Mater. Charact* 42(2-3), 203–214. doi:10.1016/S1044-5803(99)00032-7

Katona, T. J. (2013). Materials Management Strategies for VVER Reactors. *Mater. Ageing Degrad. Light Water React. Mech. Manag.*, 335–384. doi:10.1533/9780857097453.3.335

Kweon, H. D., Kim, J. W., Song, O., and Oh, D. (2021). Determination of True Stress-Strain Curve of Type 304 and 316 Stainless Steels Using a Typical Tensile Test and Finite Element Analysis. *Nucl. Eng. Tech.* 53, 647–656. doi:10.1016/J.NET.2020.07.014

Leide, A. J., Todd, R. I., and Armstrong, D. E. J. (2020). Measurement of Swelling-Induced Residual Stress in Ion Implanted SiC, and its Effect on Micromechanical Properties. *Acta Materialia* 196, 78–87. doi:10.1016/J.ACTAMAT.2020.06.030

Lucas, G. E. (1993). The Evolution of Mechanical Property Change in Irradiated Austenitic Stainless Steels. *J. Nucl. Mater.* 206, 287–305. doi:10.1016/0022-3115(93)90129-M

Mao, K. (2019). *Influence of Irradiation and Laser Welding on Deformation Mechanisms in Austenitic Stainless Steels*. doi:10.25394/PGS.8983583.V1

Mao, K. S., Sun, C., Huang, Y., Shiau, C.-H., Garner, F. A., Freyer, P. D., et al. (2019). Grain Orientation Dependence of Nanoindentation and Deformation-Induced Martensitic Phase Transformation in Neutron Irradiated AISI 304L Stainless Steel. *Materialia* 5, 100208. doi:10.1016/j.mtla.2019.100208

Mao, K., Maxim, G., Massey, C., Unocic, K., Edmondson, P., and Field, K. (2020a). *In-situ* Micromechanical Testing of Neutron Irradiated FeCrAl Alloys. *Microsc. Microanal.* 26, 646–647. doi:10.1017/s1431927620015391

Mao, K. S., Sun, C., Liu, X., Qu, H. J., French, A. J., Freyer, P. D., et al. (2020b). Effect of Laser Welding on Deformation Mechanisms in Irradiated Austenitic Stainless Steel. *J. Nucl. Mater.* 528, 151878. doi:10.1016/j.jnucmat.2019.151878

Mao, K. S., Sun, C., Shiau, C.-H., Yano, K. H., Freyer, P. D., El-Azab, A. A., et al. (2020c). Role of Cavities on Deformation-Induced Martensitic Transformation Pathways in a Laser-Welded, Neutron Irradiated Austenitic Stainless Steel. *Scripta Materialia* 178, 1–6. doi:10.1016/j.scriptamat.2019.10.037

Mao, K. S., French, A. J., Liu, X., Wu, Y., Giannuzzi, L. A., Sun, C., et al. (2021). Microstructure and Microchemistry of Laser Welds of Irradiated Austenitic Steels. *Mater. Des.* 206, 109764. doi:10.1016/j.matdes.2021.109764

Morishima, Y., Koshiishi, M., Kashiwakura, K., Hashimoto, T., and Kawano, S. (2004). Re-weldability of Neutron Irradiated Type 304 and 316L Stainless Steels. *J. Nucl. Mater.* 329-333, 663–667. doi:10.1016/j.jnucmat.2004.04.094

Nishimura, S., Katsura, R., Saito, Y., Kono, W., Takahashi, H., Koshiishi, M., et al. (1998). Yag Laser Welding of Neutron Irradiated Stainless Steels. *J. Nucl. Mater.* 258–263, 2002–2007. doi:10.1016/S0022-3115(98)00127-5

Parish, C. M., Field, K. G., Certain, A. G., and Wharry, J. P. (2015). Application of STEM Characterization for Investigating Radiation Effects in BCC Fe-Based Alloys. *J. Mater. Res.* 30, 1275–1289. doi:10.1557/jmr.2015.32

Patra, A., and McDowell, D. L. (2013). Continuum Modeling of Localized Deformation in Irradiated Bcc Materials. *J. Nucl. Mater.* 432, 414–427. doi:10.1016/J.JNUCMAT.2012.08.021

Qin, E. W., Lu, L., Tao, N. R., Tan, J., and Lu, K. (2009). Enhanced Fracture Toughness and Strength in Bulk Nanocrystalline Cu with Nanoscale Twin Bundles. *Acta Materialia* 57, 6215–6225. doi:10.1016/J.ACTAMAT.2009.08.048

Sun, B., Lu, W., Gault, B., Ding, R., Makineni, S. K., Wan, D., et al. (2021). Chemical Heterogeneity Enhances Hydrogen Resistance in High-Strength Steels. *Nat. Mater.* 20, 1629–1634. doi:10.1038/s41563-021-01050-y

Wharry, J. P., Yano, K. H., and Patki, P. V. (2019). Intrinsic-extrinsic Size Effect Relationship for Micromechanical Tests. *Scripta Materialia* 162, 63–67. doi:10.1016/J.SCRIPTAMAT.2018.10.045

Wiezorek, J. M. K., Huang, Y., Garner, F. A., Freyer, P. D., Sagisaka, M., Isobe, Y., et al. (2014). Transmission Electron Microscopy of 304-type Stainless Steel after Exposure to Neutron Flux and Irradiation Temperature Gradients. *Microsc. Microanal.* 20, 1822–1823. doi:10.1017/S1431927614010848

Xiong, L., You, Z. S., and Lu, L. (2016). Enhancing Fracture Toughness of Nanotwinned Austenitic Steel by thermal Annealing. *Scripta Materialia* 119, 55–59. doi:10.1016/J.SCRIPTAMAT.2016.03.024

Xiong, L., You, Z. S., Qu, S. D., and Lu, L. (2018). Fracture Behavior of Heterogeneous Nanostructured 316L Austenitic Stainless Steel with Nanotwin Bundles. *Acta Materialia* 150, 130–138. doi:10.1016/J.ACTAMAT.2018.02.065

Yamada, H., Kawamura, H., Nagao, Y., Takada, F., and Kohno, W. (2006). Mechanical Properties of Weldments Using Irradiated Stainless Steel

Welded by the Laser Method for ITER Blanket Replacement. *J. Nucl. Mater.* 355, 119–123. doi:10.1016/j.jnucmat.2006.04.010

Yang, C., Pachaury, Y., El-Azab, A., and Wharry, J. (2022). Molecular Dynamics Simulation of Vacancy and Void Effects on Strain-Induced Martensitic Transformations in Fe-50 at.% Ni Model Concentrated Solid Solution alloy. *Scr. Mater.* 209, 114394. doi:10.1016/J.SCRIPTAMAT.2021.114394

Yano, K. H., Wu, Y. Q., and Wharry, J. P. (2020). Method for Evaluating Irradiation Effects on Flow Stress in Fe-9%Cr ODS Using TEM *In Situ* Cantilevers. *JOM* 72, 2065–2074. doi:10.1007/S11837-020-04110-X/TABLES/2

Yasniy, P. V., Okipnyi, I. B., Maruschak, P. O., Bishchak, R. T., and Sorochak, A. P. (2011). Toughness and Failure of Heat Resistant Steel before and after Hydrogenation. *Theor. Appl. Fracture Mech.* 56, 63–67. doi:10.1016/J.TAFMEC.2011.10.001

Yasniy, P. V., Okipnyi, I. B., Maruschak, P. O., Panin, S. V., and Konovalenko, I. V. (2013). Crack Tip Strain Localisation on Mechanics of Fracture of Heat Resistant Steel after Hydrogenation. *Theor. Appl. Fracture Mech.* 63-64, 63–68. doi:10.1016/J.TAFMEC.2013.03.007

Zou, Y., Okle, P., Yu, H., Sumigawa, T., Kitamura, T., Maiti, S., et al. (2017). Fracture Properties of a Refractory High-Entropy alloy: *In Situ* Micro-cantilever and Atom Probe Tomography Studies. *Scripta Materialia* 128, 95–99. doi:10.1016/J.SCRIPTAMAT.2016.09.036

Conflict of Interest: HW was employed by the company Western Digital Corporation.

The remaining authors declare that the research was conducted in the absence of any commercial or financial relationships that could be construed as a potential conflict of interest.